Exotic FeII/FeIII local environments in the hexagonal channels of hydroxyapatite

Tiphaine Bazin, Mathieu Duttine, Isabelle Julien, Eric Champion, Alain Demourgues, Manuel Gaudon

Exotic FeII/FeIII local environments into the hexagonal channels of hydroxyapatite

Tiphaine Bazin †,‡, Mathieu Duttine †, Isabelle Julien ‡, Eric Champion ‡, Alain Demourgues †, Manuel Gaudon †,*.

† CNRS, Univ. Bordeaux, Bordeaux INP, ICMCB, UMR 5026, F-33600 Pessac, France

‡ Univ. Limoges, IRCER – Centre Européen de la Céramique, UMR CNRS 7315, F-87068 Limoges, France,

* *manuel.gaudon@u-bordeaux.fr*

KEYWORDS Structure, Mössbauer, Hydroxyapatite oxide.

ABSTRACT: In this fundamental solid state chemistry study, two sample series were deeply investigated: iron(III)-doped hydroxy-apatite (HA) compounds obtained from co-sintering process of hematite and pure HA under air and iron(III)-doped HA compounds obtained from co-sintering process from iron(II) acetate and pure HA under argon atmosphere. X-ray diffraction, UV-visible, FTIR, ^{1}H and ^{31}P NMR, , EPR and Mössbauer spectroscopies were coupled to unravel the Fe valence states, the interactions with other anionic species (OH^-, PO_4^{3-}) and finally the complex local environments into the hexagonal channels in both the two series. In particular, we highlighted the associated mechanism to ensure electroneutrality with a focus on deprotonation versus calcium substitution. From diverging mechanisms, Fe^{3+} and Fe^{2+} ions take place into different coordinated sites: 4(+1) coordinated-site for Fe^{3+}, 2(+3) coordinated site for Fe^{2+}, are clearly associated to very different Mossbauer and EPR signatures either as various absorption bands (leading to different sample colors).

1. Introduction.

Calcium hydroxyapatite (HA), a key phosphate with general formula $Ca_{10}(PO_4)_6(OH)_2$, is of great interest in bone reconstruction due to its biocompatibility and bioactivity. However, its osteoconductive properties would have to be largely improved in order to facilitate the osteointegration of large size scaffolds. The HA structure, with $P6_3/m$ space group (Figure 1) exhibits two tunnels along the *c* unit-cell axis into the apatite lattice, free from PO_4^{3-} phosphate units, which allow the substitution of the calcium ions, protons and/or the oxygen anions by various anionic groups as well as cationic dopants. The two first tunnels (tunnels I) are each filled by two calcium ions (at level z = 0 and z = 0.5), called Ca(1), which are nine-fold coordinated (D_{3h} point group symmetry, 3+3+3) to the oxygen atoms of the phosphate groups called O(3). The six other calcium atoms form two triangles at levels z = 0.25 and 0.75 leading to a hexagonal-axis tunnel (tunnel II). These calcium atoms, called Ca(2), are seven-fold coordinated to six oxygen atoms of the phosphate groups O(3) and one oxygen of the hydroxyl groups, named O(4), located at the centre of the tunnel vertical axis, *i.e.* in the centre of each triangle formed by the calcium ions [1]–[3]. The hydroxyl groups along the *c* axis (Figure 1, right inset) are labile and may move easily to accept the presence of additional elements. Therefore, doping HA with trace elements, naturally present in the body and recognized for their biological properties, is one of the main routes studied in the literature.

For instance, lithium, zinc, strontium and manganese promote the osteogenesis while magnesium, copper and cobalt improve the angiogenesis [4]. Iron is also widely used in the biomedical field, especially in hyperthermia or as contrast agent in MRI. Recently, it has been demonstrated that electromagnetic stimulations of magnetic iron-doped nanoparticles would stimulate osteogenesis [5]. Therefore, this study focuses on the incorporation of iron into HA.

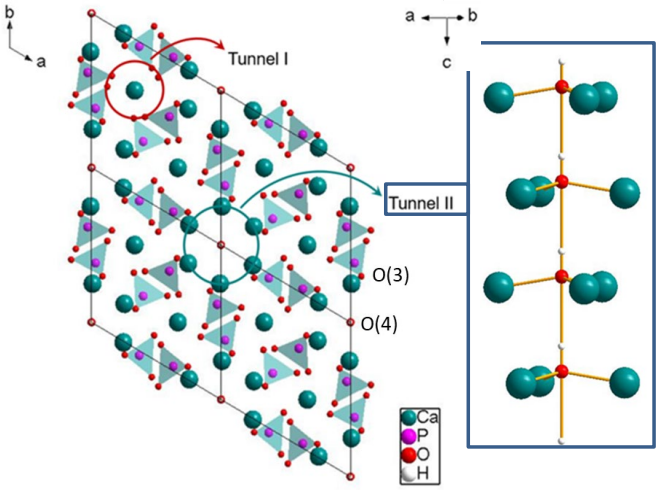

Figure 1: Crystallographic structure of hydroxyapatite: 4 unit-cells from c axis projection and focus on the Tunnel II (insert).

In the literature, iron-doped HA (FeHA) have been mainly synthetized by coprecipitation considering a ratio (Ca+Fe)/P = 10/6, *i.e.* directing the preparation through the substitution of a part of the calcium cations with iron cations. Pure FeHA phases have been obtained after thermal treatment at low temperature (< 600°C) [2], [6]–[16]. The substitution of calcium by ferrous or ferric ions, both presenting smaller ionic radii: $r(Ca^{2+})$ = 0.99 Å; $r(Fe^{2+})$ = 0.77 Å; $r(Fe^{3+})$ = 0.65 Å in six-fold coordination, should lead to a reduction of the apatite lattice parameters. However, the evolution of the lattice parameters with iron concentration varies depending on the authors: Wu *et al.* [15] observe an increase of both *a* and *c* parameters whereas the exact contrary is noted by Gamal *et al.* [6]. Others have shown the *a* parameter increase and the *c* parameter decrease versus doping concentration [8], [10], [13]. These contradictory results are probably due to the different

sample preparations and/or the different iron oxidation states. Indeed, $Fe(NO_3)_3$, $FeCl_2$ or $FeCl_3$ have been used as iron precursors. In addition, the iron insertion sites and Fe valence states are still not clearly established even through some structural studies, such as Rietveld analysis, electron paramagnetic resonance (EPR) or Mössbauer spectroscopy, have been performed. Mainly, an iron substitution for the two Ca(1) and Ca(2) sites have been reported, but different coordination numbers for the iron cations have been found [2], [8], [10], [17]. Finally, FeHA samples synthetized by coprecipitation are not thermally stable above 600°C (formation of tricalcium phosphate is then detected); unfortunately, this low thermal stability prevents the design of pure FeHA ceramics for bone reconstruction.

The incorporation of iron(III) was also considered by solid-state reaction. Salviulo *et al.* [18] observed the formation of secondary phases considering a ratio (Ca+Fe)/P = 10/6 while Kato *et al.* [19] obtained a pure FeHA phase, checked by XRD after a thermal treatment at 1150°C under air for a ratio Ca/P = 10/6 with $Ca_{10}(PO_4)_6$-Fe_xO_y (x=0.1-1) general formulae. In the latter case, a powder XRD Rietveld analysis has shown iron incorporation into the apatite structure at the 12i general position (0.12, 0, 0) corresponding to a highly distorted site four-fold coordinated to oxygens. This position is located inside the hexagonal channel of HA (tunnel II), between the triangles formed by the atoms of calcium Ca(2). The increase in the lattice volume (with *a* unit-cell parameter decreasing and *c* increasing) is in agreement with the insertion of the dopant into the structure. By FTIR spectroscopy, the intensity of ν(OH) vibration bands suggests the substitution of hydrogen atoms while a new band associated to FeO polyhedron also appears at 700 cm^{-1}. Despite the presence of secondary phases, the evolution of the apatite lattice parameters as well as the iron location was confirmed by Gomes *et al.* [20] who proceeded for the FeHA preparation from a sol-gel route followed by a thermal treatment at 1100°C. According to the XRD and ^{57}Fe Mossbauer analyses, calcium vacancies have also to be considered for the electronic charge compensation where iron atoms are located in three different environments with a coordination number equal to or less than four. However, the two-fold coordination they have proposed is particularly unusual for iron(III).

Solid-state reaction using a ratio Ca/P = 10/6 appears to be the best path to synthetize pure and thermally stable iron-doped HA, at least for the incorporation of iron(III). In the literature, only ferric ions were used as precursors and none of the authors have performed a complete structural analysis evidencing Fe organization at local scale. Therefore, this paper focuses on the solid-state synthesis of iron(II)- or iron(III)-doped HA according to the general formula $Ca_{10}(PO_4)_6Fe_xO_yH_z$. Characterizations of the different as-prepared materials (using iron(II) precursor, iron(III) precursor, and varying the atmosphere and the temperature of the sintering treatment) through several spectroscopic techniques have been carried out in order to establish the influence of the dopant on the apatite structure, the peculiar or general Wyckoff position, its local environment (coordination, site distortion...) and to verify the iron oxidation state.

2. Experimental.

2.1. Sample preparation

Stoichiometric hydroxyapatite synthesis. Pure hydroxyapatite was first synthesized by a precipitation method detailed in previous work [21]. Briefly, a solution of diammonium hydrogen phosphate $(NH_4)_2HPO_4$ (1.55 M, 1.2 L; Fisher Scientific) was dropwise added under stirring to a calcium nitrate solution $Ca(NO_3)_2.4H_2O$ (1.31 M, Sigma-Aldrich). The precipitation temperature was fixed at 85°C and the pH of the suspension, fixed at 8.5, was maintained by addition of ammonium hydroxide NH_4OH (Fisher Scientific). The solution was refluxed under argon atmosphere in order to prevent the carbonation of HA and was ripened for 5 hours after total addition of the phosphate solution. The precipitate was extracted from centrifugation, washed with distilled water and dried over nigratet 100°C. The as-prepared powder was then annealed at 600°C for 1 hour. The purity and the stoichiometry of the phase have been verified by thermal treatments above 1000°C under air (supplementary data S1).

Fe-doped HA synthesis. Fe^{III}- and Fe^{II}-doped HA samples were synthetized by solid-state reaction using respectively hematite α-Fe_2O_3 and iron(II) acetate $Fe(CH_3COO)_2$ as precursors. Stoichiometric hydroxyapatite and the precursor were intimately mixed and milled by attrition (NETZSCH device) to obtain a homogeneous mixture of sub-micrometric grains. Different precursor amounts were added leading to an iron content x = 0.25; 0.5 or 1.0 in respect of the general formula: $Ca_{10}(PO_4)_6Fe_xO_yH_z$. Milling step was carried out at 800 rpm for 3 hours in a Teflon ball containing distilled water, yttrium-stabilized zirconia balls of 1 mm diameter and 1 wt% of dispersant Darvan CN (Vanderbilt Minerals) towards the total amount of powders. The suspension was then dried over night at 100°C and sieved at 80 µm. Green pellets were shaped by uniaxial pressing at 100 MPa and sintered from 1000 to 1400°C with a dwell time of 1 hour and a heating rate of 10°C.min^{-1}. Pellets containing ferric ions were calcined under air while those containing iron(II) were calcined under argon atmosphere in order to avoid the oxidation of ferrous ions. The pellets were grinded for further characterizations.

2.2 Characterization techniques

Powder X-Ray diffraction (XRD). Purity of the phases was verified by XRD using a diffractometer Bruker D8 Advance Serie II equipped with a CuKα1 radiation X-ray tube and a rear monochromator. Patterns were collected at 40 kV and 40 mA between 10 and 60° (2θ) with a step size of 0.02° and a time per step of 1.2 s. Samples were rotated at 10 rpm in order to increase the counting statistics.

The crystallographic structure of the iron-doped phases was refined by Rietveld analysis using FullProf software. At the exception of the step time, fixed now at 19 s, the same conditions as previously were used to collect the patterns. After each refinement, the corresponding structural networks were drawn thanks to Diamond software.

Optical properties. The optical properties of the samples were evaluated by diffuse reflection. Spectra were recorded between 200 and 2500 nm using a UV-visible-IR spectrometer Cary 5000 (Varian) equipped with an integrating sphere. They were then transformed according to the Kubelka-Munk

relation: $K/S = (1-R)^2/2R$ with K, S and R respectively the absorption, scattering and reflection coefficients.

Fourier transform infrared spectroscopy (FTIR). Infrared spectra were obtained on a Spectrum One FTIR spectrometer from Perkin Elmer. A number of 32 scans was recorded between 4000 and 400 cm^{-1} with a 4 cm^{-1} resolution using the KBr pellet method.

NMR spectroscopy. ^{1}H and ^{31}P Solid-State nuclear magnetic resonance (NMR) analyses were carried out on a Bruker Avance III 300 WB spectrometer (B0 = 7.05 T). Experiments were performed under Magic Angle Spinning (MAS) conditions (30 kHz) with a rotor-synchronized Hahn-echo pulse sequence (90° - 180°) with a 90° pulse length of 2 µs and an optimized recycle delay (ranging from 0.5 s to 700 s depending on the analyzed samples and the probed nuclei). The chemical shift scale was calibrated using H_2O milliQ ($\delta(^1H)$ = +4.7 ppm) or phosphoric acid H_3PO_4 ($\delta(^{31}P)$ = 0 ppm) as reference.

EPR spectroscopy. Electron paramagnetic resonance spectra were recorded from room temperature down to 10K using a X-band (9.54 GHz) Bruker ESP300E spectrometer equipped with liquid helium flow cryostat. The main parameters set for the experiments were 10 mW microwave power, a magnetic field modulation with 100 kHz frequency and 1 mT amplitude and a 82 ms conversion time. A DPPH ((2,2)-diphenyl-1-picrylhydrazyl) sample was used as external reference (g = 2.0036).

^{57}Fe Mössbauer spectroscopy. Experiments were performed in transmission geometry with a constant acceleration (Halder-type) spectrometer equipped with a $^{57}Co(Rh)$ radioactive source at room temperature. Mössbauer spectra were recorded at 100 K using thin absorbers with iron concentration of about 1 $mg.cm^{-2}$ placed into a liquid nitrogen bath cryostat. The Mössbauer hyperfine parameters (δ isomer shift, Δ quadrupole splitting, Γ Lorentzian linewidth) and relative area of each component were refined with the WinNormos software (Wissenschaftliche Elektronik GmbH). Isomer shifts are given with respect to metallic iron (α-Fe) at room temperature. .

Results and discussion.

Two sample series were studied. The first sample series, obtained from co-sintering process of hematite and pure HA (see experimental part) under air can be reasonably supposed, in first approximation, such as iron(III)-doped compounds whereas the second sample series, obtained from co-sintering process from iron(II) acetate and pure HA under argon atmosphere can be reasonably supposed iron(II)-doped compounds. In both the two compound series, three different iron contents were studied x_{Fe} = 0.25, x_{Fe} = 0.5 and x_{Fe} = 1.0 regarding the general formula $Ca_{10}(PO_4)_6Fe_xO_yH_z$. Thus, the synthesized compounds are included among five different target chemical compositions which are named hereafter Fe^{III}(¼)HA, Fe^{III}(½)HA, Fe^{III}(1)HA, Fe^{II}(¼)HA, and Fe^{II}(1)HA.

The purity of the FeHA phases has been checked by X-Ray diffraction. The XRD patterns of the two compounds containing an amount of dopant x_{Fe} = 0.25 (Fe^{III}(¼)HA, Fe^{II}(¼)HA) are discussed first (Figure 2).

In presence of iron(III) (Figure 2a), pure apatite phases have been obtained using thermal treatment between 1100 and 1300°C, for 1 hour. The precursor Fe_2O_3 is still identified after calcination at 1000°C while a low amount of α-tricalcium phosphate (α-TCP) appears at 1400°C. Pellets, with a light maroon color, turns into a brown color with the increase of temperature. When iron(II) is used as a precursor, the change of color is less obvious and a pure apatite phase is obtained whatever the calcination temperature may be (Figure 2b).

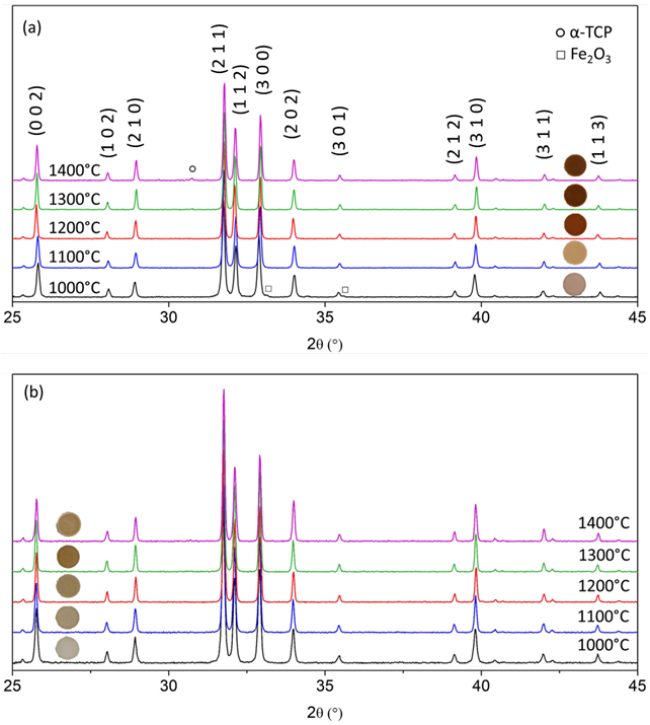

Figure 2: X-ray diffraction patterns on Fe^{III}(¼)HA (a), Fe^{II}(¼)HA (b) compounds.

For comparison, XRD patterns of the powders doped with the highest iron content (Fe^{III}(1)HA (a), Fe^{II}(1)HA, Figure 3), reveal the same tendencies that the ones observed for x_{Fe} = 0.25, but the demixing phenomena occurring at high temperatures are even more visible at high iron content. The sample prepared from iron(III) precursor at 1400°C contains as much calcium phosphate (α-TCP) as hydroxyapatite while a pure apatite phase is obtained in the case of ferrous ions whatever the temperature may be (only traces of α-TCP are detected at 1400°C). These observations already support a partial substitution of calcium(II) by iron(III) (causing the α-TCP formation) and additional reactions with iron precursor excess, whereas the iron(II) appears in interstitial sites into the lattices rather than in substitution for calcium. Therefore, the incorporation of iron(III) into HA seems to lead to its destabilization above a certain amount of dopant and a certain temperature.

The differences of behavior between ferric and ferrous ions are also supported by the evolution of the FeHA lattice parameters versus the annealing temperature (Figure 4 for iron(III)-doped HA and Figure 5 for iron(II)-doped HA).

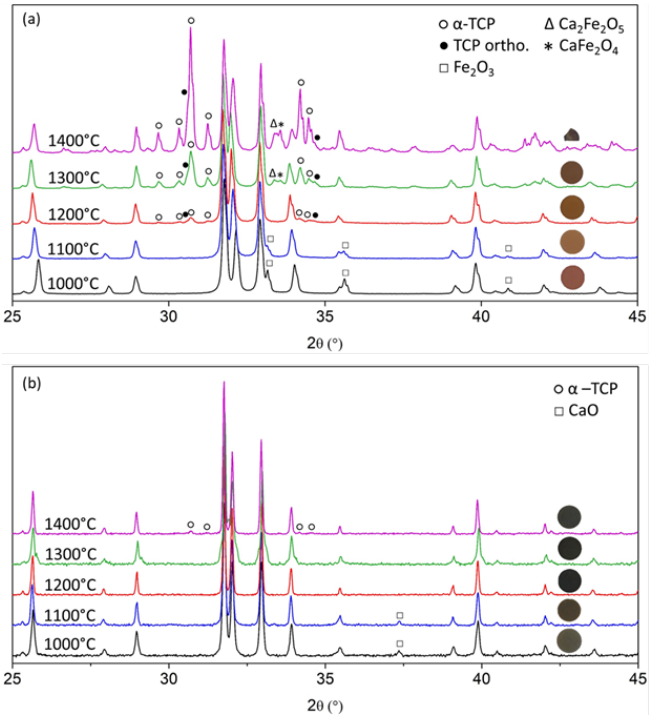

Figure 3: X-ray diffraction patterns on Fe^{III}(1)HA (a), Fe^{II}(1)HA (b) compounds.

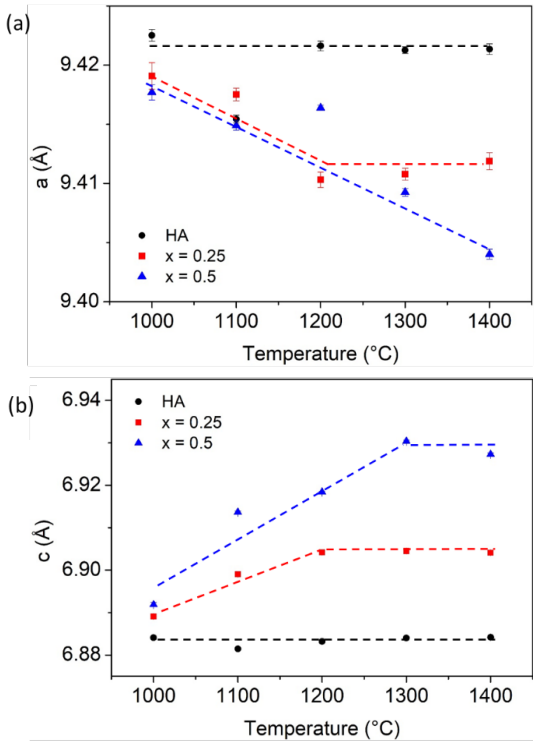

Figure 4: Evolution of the unit-cell lattice parameters *vs* annealing temperatures of the pure HA, Fe^{III}(¼)HA and Fe^{III}(½)HA: *a* unit-cell parameter (a) and *c* unit-cell parameter (b).

For a fixed iron(III) concentration, the *a* unit-cell parameter decreases and the *c* unit-cell parameter increases before stabilizing versus the annealing temperature. The increase of unit-cell parameters can be related to gradual incorporation of iron species inside the HA framework; while *a* and *c* parameters do not vary with the annealing temperature, it means the Fe cations in specific valence states reached thermodynamically stable positions in the HA framework. Hence, the *a* and *c* unit-cell parameter plots versus annealing temperature illustrate the Fe^{3+} or Fe^{2+} incorporation versus annealing temperature.

In contrast, in presence of Fe^{2+} ions as dopants, both lattice parameters are constant on the whole range of studied annealing temperatures (Figure 5). So the ferrous ions can be supposed to be inserted more easily than the ferric ones, in HA crystallographic structure, even after low annealing temperature.

In addition, it can be noted that the increase of the apatite lattice volume in both cases (i.e. for iron(III) as well as iron(II)-doped FeHA samples) has been observed. The unit-cell increase with iron(III) incorporation is very anisotropic (a decreases while c parameter increases, comparing x_{Fe} = 0, 0.25 or 0.5) while is more important and isotropic with iron(II) incorporation (both a and c parameters increase comparing x_{Fe} = 0, 0.5 and 1).

These different observations already presume a different location into HA framework for Fe^{2+} and Fe^{3+} ions.

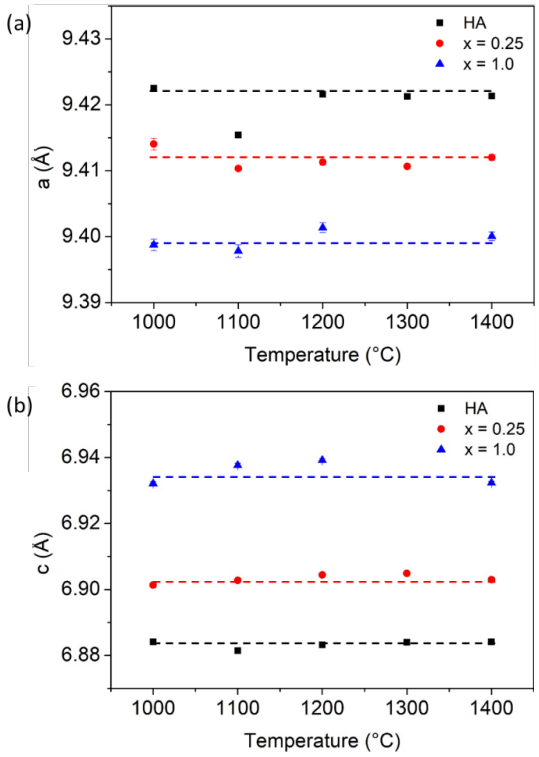

Figure 5: Evolution of the unit-cell lattice parameters: *a* parameter (a) and *c* parameter (b) of the pure HA, Fe^{II}(¼)HA (a), Fe^{II}(1)HA.

To investigate more deeply the iron location in the apatite lattice, the samples containing the lowest amount of iron (Fe^{III}(¼)HA and Fe^{II}(¼)HA) obtained after thermal treatment at 1200°C were thoroughly studied. As a reminder, Fe^{III}(¼)HA and Fe^{II}(¼)HA have been obtained as pure apatite phases.

The optical properties of the as-prepared Fe^{III}(¼)HA and Fe^{II}(¼)HA powders are commented thanks to the diffuse

reflectance spectra, plotted using Kubelka-Munk coordinates (Figure 6). The Fe^{II}(¼)HA powder exhibits an absorption band at 9765 cm^{-1} (1024 nm or 1.21 eV) which is characteristic of electronic transitions between the *3d* orbitals of iron(II) in octahedral site. Indeed, considering in first approximation that the energy of 1.21 eV is well due to the crystal field splitting (t_{2g} / e_g orbital splitting), this value is close to the energy measured in the $Fe(H_2O)_6^{2+}$ octahedral complex (equal to 1.24 eV or 10 000 cm^{-1}), absorption band being associated to the *d-d* transition $^5T_2 \rightarrow {}^5E$ [22].

Therefore, the environment of the ferrous ions into the apatite structure seems to be close to an octahedral site with oxygens as ligands. Regarding the Fe^{III}(¼)HA, the band at 20 900 cm^{-1} (480 nm) could be due to interatomic charge transfer (O → Fe) associated to iron(III) in a tetrahedral site [23] . The presence of shoulder-peaks at 14 600 et 19 200 cm^{-1} is in agreement with the expected *d-d* transitions for a low crystal field, such as a tetrahedral field close to 1 eV (7936 cm^{-1}) with a Racah parameter B around 600 cm^{-1} corresponding to $^6A_1 \rightarrow {}^4T_1$ and $^6A_1 \rightarrow {}^4A_1$ electronic transitions at 14 400 cm^{-1} and 19 200 cm^{-1}, respectively. The third expected transition $^6A_1 \rightarrow {}^4T_2$ at 18 000 cm^{-1} is however less visible. Therefore, Fe^{2+} and Fe^{3+} ions seem to be located in two very different environments.

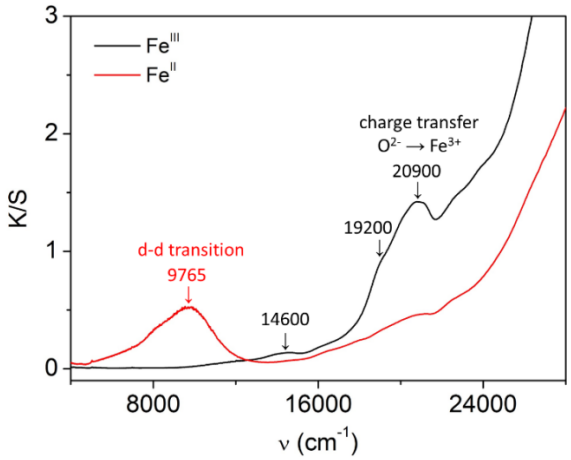

Figure 6: Diffuse reflectance spectra (Kubelka-Munk K/S coordinates) of Fe^{III}(¼)HA and Fe^{II}(¼)HA compounds obtained after annealing at 1200°C.

The impact of iron doping on the local environments of protons and phosphate groups in the HA structure was then investigated by FTIR and Solid-State NMR spectroscopies (Figure 7) through the comparison of a pure undoped HA and two iron-doped HA compounds (Fe^{III}(¼)HA and Fe^{II}(¼)HA annealed at 1200°C). Compared to the undoped HA compound, the FTIR spectra of both iron-doped HA samples clearly show a decrease of the 630 and 3570 cm^{-1} bands along with the appearance of two new bands at about 680 and 990 cm^{-1}. The decrease of the first two bands, which are associated with hydroxyl groups, suggests that a part of the H^+ ions was substituted by Fe^{2+} or Fe^{3+} ions. Furthermore, the OH^- groups seems to be more affected by the presence of ferrous ions as an additional strectching vibration band is detected at 3350 cm^{-1}.The incorporation of iron into the apatite structure is also supported by the detection of a new bending vibration band at 680 cm^{-1} which is related to the formation of Fe-O polyhedra [24]–[26] and a broad stretching vibration band at about 990 cm^{-1} which has already been reported for iron phosphates [27]–[29]. Finally, the band at 430 cm^{-1}, already observed in FTIR spectra of oxy-hydroxyapatites [30], may be associated with PO_4 groups close to O^{2-} ions.

The ^1H MAS NMR spectrum of the undoped HA sample (Figure 7b) mainly exhibits a sharp and intense resonance line associated with hydroxyl groups and characterized by an isotropic chemical shift $\delta_{iso} = 0.05$ ppm and a long T_1 relaxation time (~ 50 s). The intensity of this resonance line significantly decreases as iron ions are incorporated in the hydroxyapatite lattice. The NMR spectra of both Fe^{III}(¼)HA and Fe^{II}(¼)HA compounds are mainly composed of broad and shifted signals which are associated with remaining protons in disturbed environments. [31] Furthermore, these two NMR signals are characterized by shorter relaxation times ($T_1 < 1$ s), broader resonance lines and higher isotropic shifts (+5.1 ppm and +7.0 ppm) what is consistent with the incorporation of Fe^{2+} or Fe^{3+} paramagnetic ions in the HA structure (electron spin – nuclear spin dipolar interactions and Knight shift due to the change of the global magnetic susceptibility). Phosphate groups are also strongly affected by the presence of the dopant. The intensity of the ^{31}P resonance line at 2.5 ppm associated with phosphorus atoms located into regular phosphate groups (i.e. with regular tetrahedral configuration) decreases and its line width drastically increases. This effect, which is directly related to the strong interaction between the ^{31}P nuclear spins and the unpaired electron spins of Fe^{3+} or Fe^{2+}, is more pronounced for Fe^{II}(¼)HA than for Fe^{III}(¼)HA compound. Thus, the location of Fe^{2+} ions within the HA lattice may be different from Fe^{3+} ions so that the direct or indirect dipole-dipole interactions between the unpaired electron spins and the ^{31}P nuclear spins could be stronger. Finally, for Fe^{III}(¼)HA, the intensity of the minor resonance line at 6.3 ppm, already reported in oxy-hydroxyapatite [31], increases, showing higher quantity of O^{2-} ions close to PO_4^{3-} groups.

Therefore, combining the observations made using ^1H NMR and FTIR spectroscopies, it can be clearly concluded that the incorporation of iron(II) into the apatite structure seems to lead to different interactions with hydrogen atoms, mainly related to another location of such iron(II) than in the case of iron(III) species. Furthermore, from ^{31}P NMR study, it was shown that doping HA with ferrous or ferric ions not only provokes the substitution of a part of the hydrogen atoms but also affects the phosphate group environments, this phenomenon being even more pronounced in the case of Fe^{2+} ions. Furthermore, the occurrence of Fe^{2+}-Fe^{3+} local magnetic interactions should also strongly affect the nature of such signals. These observations support the hypothesis of different environments for ferric and ferrous ions. The need to respect the charge electroneutrality is probably reached, in the FeIII case, then involving calcium vacancies, in good agreement with the α-TCP phase identified by XRD besides the Fe^{III}HA phase.

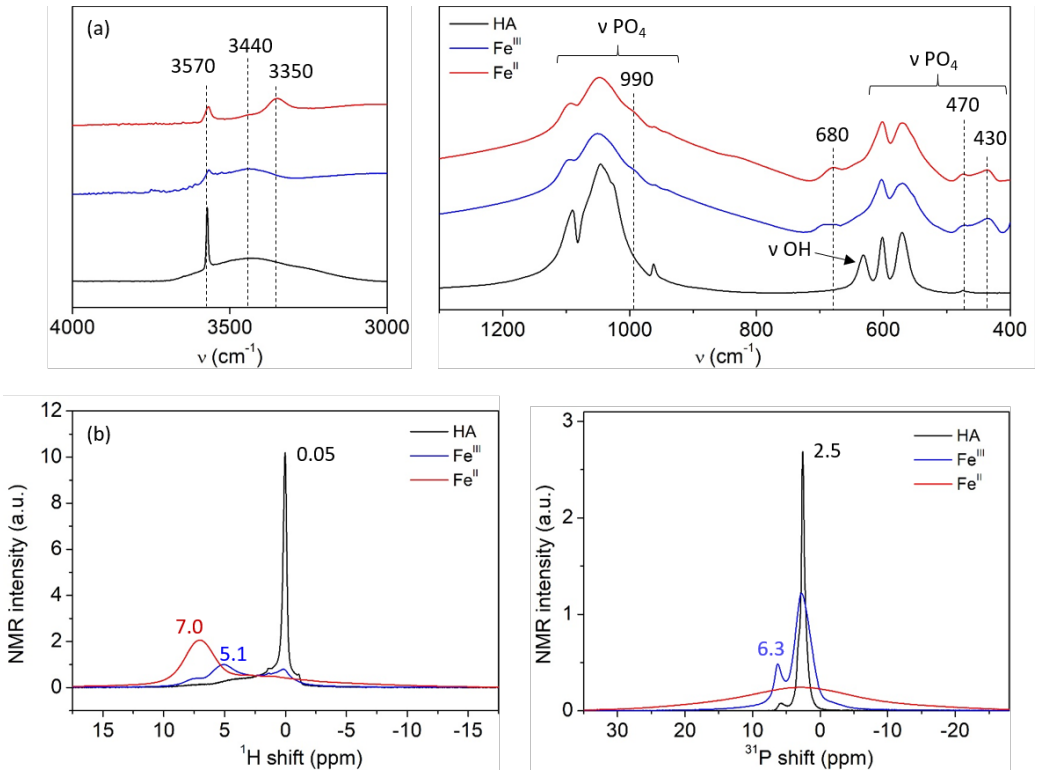

Figure 7: FTIR (a) and $^{1}H/^{31}P$ NMR (b) analyses on pure HA, Fe^{III}(¼)HA and Fe^{II}(¼)HA compounds obtained at 1200°C

Rietveld analyses have been performed to determine the atomic position of iron(II) and iron(III) into Fe-incorporated HA. Fourier difference cartographies have been extracted from the refinement made considering no iron incorporation, and from the optimal refinement in which, the iron introduction has been well considered. As for X-ray diffraction studies, a larger quantity of dopant than for NMR or FTIR spectroscopies is necessary for the detection with an adequate accuracy of this iron site. The investigations have been performed on Fe^{III}(½)HA and Fe^{II}(1)HA, relying on a lower calcination temperature than previously: 1100°C for 1 hour, in order to keep monophasic compounds.

First, the Fe^{III}(½)HA was analyzed. From the XRD pattern refinement considering no iron atom, the resulting high electronic density residues on the Fourier difference cartographies allow the location of Fe^{3+} at the 12i Wyckoff (general) position (0, 0.14, 0.47) (Figure 8a). The second refinement (illustrated in Figure 8b), carried out by adding an atom of iron at this position with refined occupancy, leads to homogeneous and low density residues less than 0.25 $e^{-}/Å^{2}$ (Figure 8a). The agreement factors R_p, R_{wp} and R-Bragg are then respectively less than 8%, 8% and 3%. The iron occupancy (equal to 0.030 in 12i position) corresponds to an iron molar quantity of 3.6 % (Table 1) which is close to the amount measured by ICP-OES (4.3 mol.%) and the target content (5 mol.%). This confirms the presence of iron(III) species mainly located at this position. Additionally, calcium deficiency for the Ca(2) site has been noticed. The Ca(2) vacancies leads to a deficit of 3 mol.% regarding the whole calcium content which well corresponds well to the amount of incorporated iron in the apatite structure and leads to the theoretical formula $Ca_{9.7}(PO_4)_6Fe_{0.3}O_yH_z$. Therefore, at this stage, considering the FTIR, NMR and XRD results, it can be already supposed that each iron(III) ion may substitute one proton and one calcium atom into the apatite structure, with respect of the mineral solid electroneutrality.

Secondly, regarding the Fe^{II}(1)HA compound, considering no iron incorporation, the highest electronic density residues have been identified at the 2b Wyckoff position (0, 0, 0.25) (Figure 9a). After adding an atom of iron at this position, the remaining main residues are located at the same position than the ferric ions (0, 0.14, 0.45) (Table 2) in the Fe^{III}(1)HA compound.

Thus, a partial oxidation of the Fe^{2+} ions into Fe^{3+} ions, that may occur during the thermal annealing treatment should be taken into account. Indeed, basing on the oxidation from FeO to Fe_3O_4 (Ellingham plot), very low oxygen partial pressure (10^{-5} – 10^{-8}) can produced easily for 1000-1400°C annealing temperatures a partial ferrous to ferric ions oxidation. So, argon flow can be oxidant atmosphere. The agreement factors R_p, R_{wp} are about 15 % while the R-Bragg factor is 7.2% (Figure 9b). In addition, the occupancy measured on the 2b position, leads to an equivalent molar content of 6.2 mol%, lower than 9.3 mol.% titrated by ICP-OES and expected 10 mol.%. Therefore, ferrous or ferric ions in minor quantities are also located at other atomic positions such as (0, 0.14, 0.45) one's previously mentioned.

The positions of the Fe^{3+} and Fe^{2+} ions in the iron(III) and iron(II)-doped HA compounds are reported in Figure 10.

Firstly, Fe^{3+} ion, with 12 equivalent positions, is located between the calcium Ca(2) triangles, inside the tunnel II of the HA structural network (Figure 10a). Considering the too short cation-cation distances (< 2 Å) observed between the iron dopant and the first neighboring hydrogen and between iron dopant and the first neighboring calcium atom, we assumed

that these Ca^{2+} and H^+ ions are substituted by Fe^{3+} ions to respect the electroneutrality of the apatite structure, in agreement with the previous hypotheses. Rietveld analysis gives access to the average atomic position over the whole structure but locally the anionic position surrounding the interstitial iron ion must be modified in order to adapt the Fe^{3+} ionic radius and to satisfy the Fe^{3+} - O^{2-} bond valences. Depending on the z value of iron and oxygens, two situations are possible: the Fe^{3+} substituting for Ca^{2+} can be close to either the hydroxyl group or the O^{2-} ion (Figure 10 b,c). In both cases, the consideration of a slight decrease of the Fe-O(4) bond distance (from a delocalization of the oxygen atoms, which can be considered with a lability along the *c* axis) allows easily the achievement of bond valences leading to the theoretical oxidation degree +III for the interstitial iron doping ion, involving O3 oxygen atoms of PO_4 Td site. Therefore, iron(III) may be at the center of a distorted square base pyramid (coordination number = 5): two pyramid corners being located on the tunnel II central axis and three other one's belonging to the phosphate groups. Iron(III) could also be considered as in a tetrahedral site since one of the Fe-O bond valence is close to zero (0.05). In addition, in Figure 8b, the calculated O^{2-}(4) valence is -1.74 and -2.05 for O^{2-}(4) linked to H^+ whereas in Figure 8 the calculated valence of two O^{2-} (4) are equal to -2.01 (linked to H+) and to -2.03. A more complex reorganization of the atoms surrounding iron, especially of the oxygen atoms O(3) associated to PO_4 groups, could occur to satisfy all oxidation degrees.

Secondly, in the case of iron(II) ions into $Fe^{II}HA$ compound, two hydrogen atoms have been substituted in respect of the apatite electroneutrality (Figure 10d). The position of the Fe^{2+} ion can be described as a nearly regular linear di-coordinated site oriented along *c* axis; nonetheless, three additional oxygens at larger bond lengths (bond valence equal to 0.03) may be also taken into account for the first coordination sphere consideration of such Fe^{2+} ion. All in all, the interstitial Fe^{2+} site can be considered as [2+3] coordinated. By moving the two first neighboring oxygens along the *c* axis, it is possible to obtain Fe-O bond valences which are perfectly leading to the iron oxidation state +II. However, it can be noted that the two Fe-O bond lengths are then very short (1.75 Å) with too low calculated valence of O(4) ions around -1.50. This exotic linear coordination for iron metal ion strongly argues for the displacement of the phosphate groups closer to the tunnel central axis allowing the oxygen atoms of the PO_4^{3-} groups to well participate to the coordination sphere of the dopant leading to a rather standard Fe^{2+} five-fold coordination. This structural reorganization of Fe local environments into HA matrix is supported by the evolution of the lattice parameters, especially by the decrease of the *a* parameter.

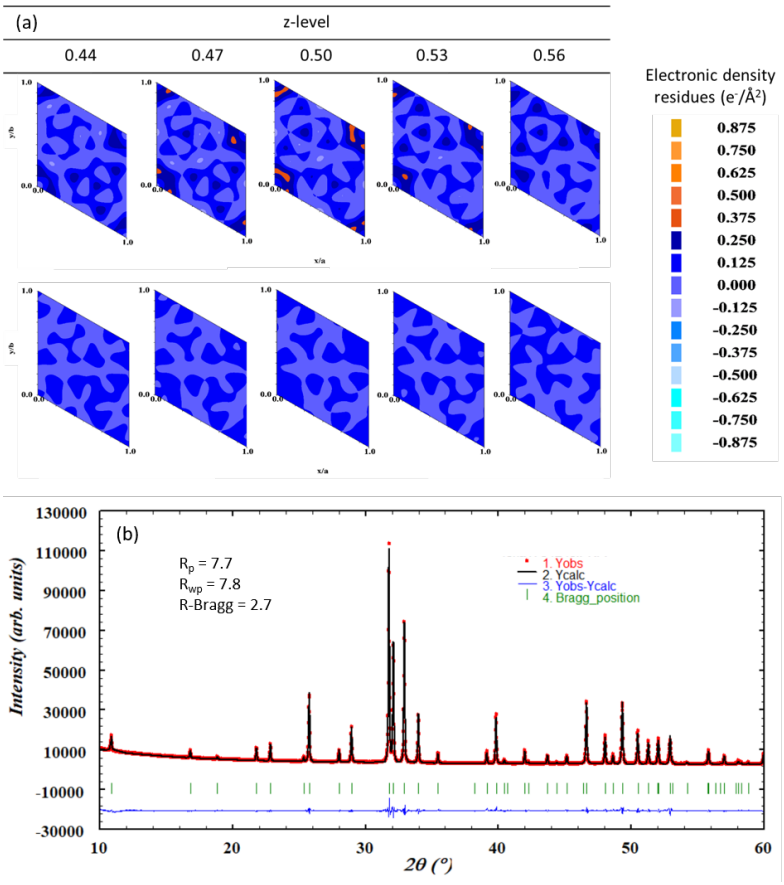

Figure 8: Fourier difference cartographies obtained from Rietveld analysis of the Fe^{III}(½)HA obtained after annealing at 1100°C without (top line) or with (bottom line) consideration of iron(III) atom (a). XRD pattern refinement result considering iron(III) atom located on (0, 0.14, 0.45) position (b).

Table 1: Atomic positions and occupancy rates obtained from Rietveld refinement of the XRD pattern of the Fe^{III}(½)HA phase considering iron(III) atom located on (0, 0.14, 0.45) position.

	Atom	Site	x	y	z	B_{iso}	Occ
Fe^{III}HA	Ca1	4f	1/3	2/3	0.001(1)	0.5	1
$P6_3/m$	Ca2	6h	0.2472(6)	0.9924(7)	1/4	0.5	0.95(1)
a = 9.4129(4) Å	P1	6h	0.3966(9)	0.367(1)	1/4	0.5	1
c = 6.9118(3) Å	O1	6h	0.325(2)	0.484(2)	1/4	1.0	1
V = 530.36(4) $Å^3$	O2	6h	0.585(2)	0.464(2)	1/4	1.0	1
	O3	12i	0.339(1)	0.254(1)	0.072(1)	1.0	1
	O4	4e	0	0	0.201(5)	1.0	1/2
	H1	4e	0	0	0.0582	2.0	1/2
	Fe1	12i	0	0.143(8)	0.45(1)	0.5	0.030(2)

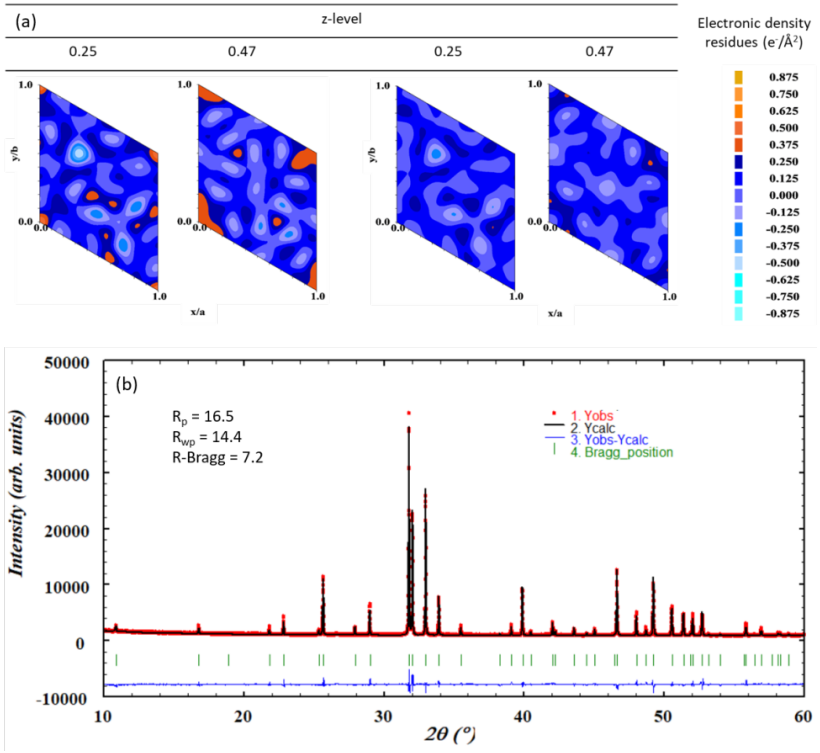

Figure 9: Fourier difference cartographies obtained from Rietveld analysis of the Fe^{II}(1)HA obtained after annealing at 1100°C without (top line) or with (bottom line) consideration of iron(III) atom (a). XRD pattern refinement result considering iron(III) atom located on (0, 0.14, 0.45) position (b).

Table 2: Atomic positions and occupancy rates obtained from Rietveld refinement of the XRD pattern of the Fe^{II}(1)HA phase considering iron(II) atom located on (0, 0, 0.25) position.

	Atom	Site	X	y	z	B_{iso}	Occ
Fe^{II}	Ca1	4f	1/3	2/3	0.001(1)	0.5	1
$P6_3/m$	Ca2	6h	0.2461(7)	0.9929(8)	1/4	0.5	0.968(3)
a = 9.40(4) Å	P1	6h	0.396(1)	0.366(1)	1/4	0.5	1
c = 6.9118(3) Å	O1	6h	0.330(2)	0.489(2)	1/4	1.0	1
V = 530.36(4) $Å^3$	O2	6h	0.581(2)	0.461(2)	1/4	1.0	1
	O3	12i	0.343(1)	0.256(1)	0.071(1)	1.0	1
	O4	4e	0	0	0.0873(5)	1.0	1/2
	H1	4e	0	0	0.0582	2.0	1/2
	Fe1	2b	0	0	0.25	0.5	0.186(2)

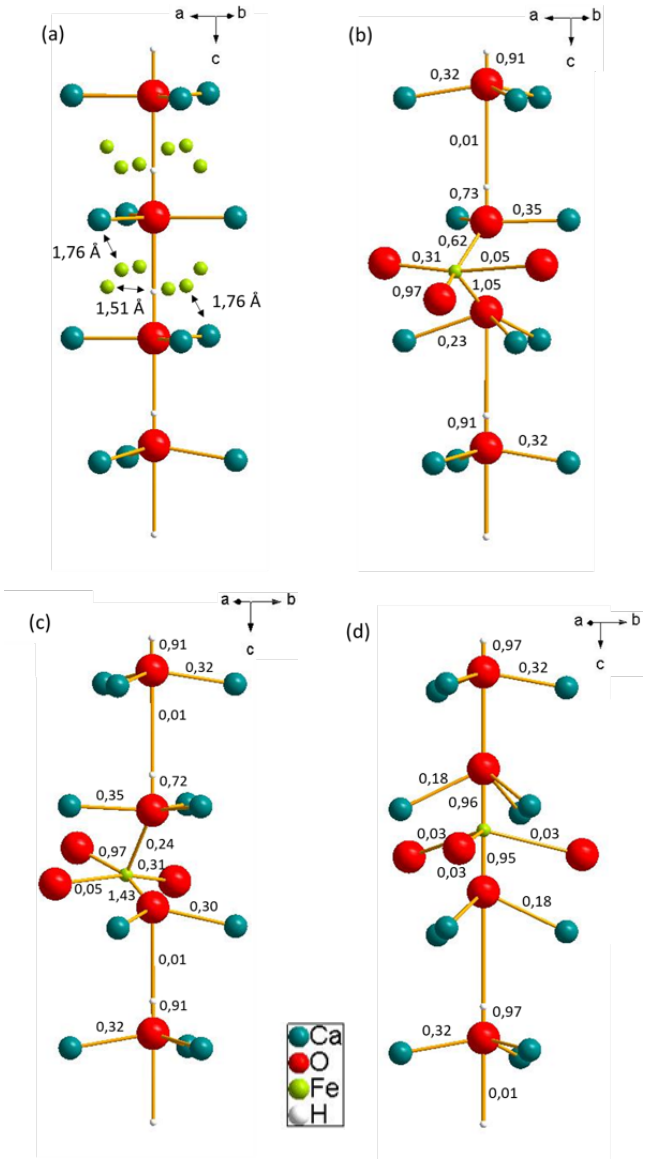

Figure 10: The 12 equivalent positions of Fe^{3+} dopant in $Fe^{III}HA$ compounds (a), leading to the Fe^{3+} for Ca^{2+} substitution linked to the hydroxyl group (b) or to O^{2-} without protons (c). The location of Fe^{2+} dopant in $Fe^{II}HA$ compounds associated to the disappearance of two hydrogen atoms (d). The values indicated at the chemical bond are the valence bond.

Additionally, the local environments of iron ions were studied by EPR and Mössbauer spectroscopies for the samples containing the lowest iron concentration: $x_{Fe} = 0.25$, *i.e.* the Fe^{III}(¼)HA and Fe^{II}(¼)HA compounds that were obtained after annealing treatment at 1200°C.

Conventional X-band (9.5 GHz) EPR experiments only allow to detect Fe^{3+} ions ($3d^5$, S=5/2) whereas high frequency or high field EPR spectroscopy is required to observe resonance lines associated with high spin Fe^{2+} ($3d^6$, S=2, i.e. a non-Kramer integer-spin system). The comparison of the X-band EPR spectra recorded at ambient temperature (293 K) and low temperatures (100 K and 10 K) for both Fe^{III}(¼)HA and Fe^{II}(¼)HA compounds (Figure 11) illustrates this situation: the same signals are observed for both samples but the overall EPR intensity is significantly lower for the Fe^{2+}-doped sample. All the observed signals can thus be attributed to Fe^{3+} ions. Hence, in the sample prepared from iron(II) acetate, a small amount of iron(III) is detected, due to partial oxidation during the annealing treatment, supporting the previous Rietveld analysis. Furthermore, the fact that the same EPR signals are observed for both iron-doped samples unambiguously indicates that the Fe^{3+} ions are located at very similar crystallographic sites in both HA compounds.

The EPR spectra recorded at room temperature (293 K) mainly exhibit an intense and sharp resonance line at low fields ($g_{obs.}$= 4.3) and a broad line centered at about 330 mT ($g_{obs.}$= 2.09). The EPR signal with $g_{obs.}$= 4.3 (and a shoulder at $g_{obs.}\approx 9$) is characteristic of high spin Fe^{3+} ($3d^5$, S = 5/2) in a low-symmetry environment with nearly maximal rhombicity (E/D = 1/3; E and D: zero field splitting parameters) while for a tetragonal or near tetragonal symmetry resonance lines with effective g values $g_{\perp}\approx 6$ and $g_{//}\approx 2$ are expected. [32-34] Thus, the g = 4.3 signal can be associated with Fe^{3+} ions in a distorted tetrahedral site [35-36] and the g = 5.5 resonance line with a tetragonal-pyramidal site as illustrated in Figure 10. As the broad signal at $g\approx 2$ becomes broader and shifts towards low fields as the temperature decreases and completely disappears at temperature lower than 100 K, it is probably due to some ferromagnetic FeOx clusters or Fe^{3+}-O-Fe^{3+} dimers [36-37]; hence, some iron ions are therefore close to each other into the apatite structure. Furthermore, below 30 K, an additional EPR signal with apparent axial symmetry is detected at g = 2.0. This last signal may be associated with isolated Fe^{3+} ions in a more regular and symmetrical ($D\approx 0$, $E\approx 0$) environment such as a regular tetragonal bipyramid. The fact that this signal is only detected at low temperature could arise from either a drastic increase of the spin-lattice relaxation time below 30 K or a structural rearrangement or, at least, a geometrical modification of the Fe^{3+} local environment. Indeed, X-ray diffraction analyses suggest that Fe^{3+} ions are mainly located in a 4+1 coordinated site with O^{2-} and OH^- group (Figure 10b). With such a complex geometry, an important change of the proton localization upon cooling down can drastically change the local environment of Fe^{3+} ions and then, explain the observed differences in EPR spectra between room temperature and 10 K.

In order to further investigate the local environments of both Fe^{3+} and Fe^{2+} ions in the hydroxyapatite structure, ^{57}Fe Mössbauer experiments were performed on both Fe^{III}(¼)HA and Fe^{II}(¼)HA compounds obtained after annealing at 1200°C (Figure 12). The spectra were recorded at 100 K to significantly increase the recoilless fraction or Lamb-Mössbauer factor (f) which depends on the Debye temperature and thus, improve the signal over noise ratio. Due to the difference of temperature between the gamma rays source (293 K) and the absorber (100 K) the observed signals are shifted by about +0.10 mm/s (second-order Doppler effect). The refined hyperfine parameters of the different components (quadrupole doublets, QD) are reported in Table 3. In brief, it can be reminded that the isomer shift (δ) directly depends on the electronic density within the nucleus which is determined by the spin state, the coordination number of the iron ions and also by the Fe-O bond covalency. The electric field gradient (EFG) at the iron nucleus, which arises from the anisotropic charge distribution around iron, has influence over the value of

the quadrupole splitting parameter (Δ). Thus, large distortions of iron sites and to some extent inhomogeneous distribution of first-neighbor cations lead to high Δ values. In contrast, low values of the quadrupole splitting parameter are expected for iron(III) ions in regular and symmetrical local environments (iron(II) – high spin – always has high QS because of the $3d^6$ structure). Moreover, the linewidth of the Lorentzian-shaped resonance lines gives also some information about the iron local environment. Broad lines usually reflect the occurrence of a local disorder and/or a distribution of slightly different local environments, similar crystallographic sites with small variations in distortion degree, for instance.

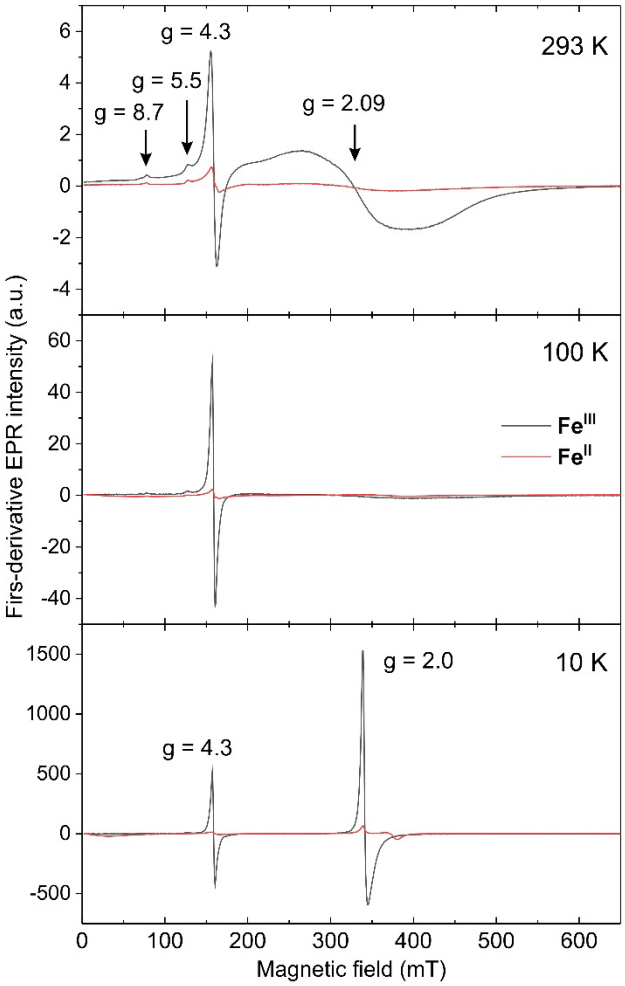

Figure 11: X-band EPR spectra of Fe^{III}(¼)HA and Fe^{II}(¼)HA compounds (annealed at 1200°C) recorded from ambient temperature down to 10 K.

The spectrum of the sample prepared from iron (III) precursor recorded at 100 K (Figure 12a) can be described with three components (quadrupole doublets) with isomer shifts equal to 0.20, 0.34 and 0.39 mm/s (at 100 K). They are associated without any ambiguities with high spin Fe^{3+} ions in different environments. The difference in isomer shift value is attributed to different coordination numbers. Considering the XRD results, the doublets with the isomer shifts 0.34 and 0.39 mm/s are attributed to iron(III) respectively in four-fold and five-fold coordination (Figure 10b and 10c, respectively) [38]. Furthermore, the high values of the quadrupole splitting parameter of the QD2 and QD3 doublets (> 1.5 mm/s) clearly reflect the large distortion of both iron sites, in good agreement with the XRD results. The QD1 component with a low value of the isomer shift parameter (0.20 mm/s) is unusual for iron (III). It may be attributed to an exotic very low [2+x] coordination number [39]. This site could be deducted from the Fe^{3+} position (0, 0.14, 0.47) by moving some of the oxygen atoms a bit away, *i.e.* it can be proposed a reorganization of the interstitial site geometry based on the consideration that only the two oxygen atoms located in the centre of the tunnel I, being the nearest oxygen atoms for iron, remain in the first coordination sphere of iron. Therefore, iron(III) could be situated either in different sites, or in the same insertion site with different environments by adjusting in different ways the surrounding oxygen positions, thus leading to several coordination numbers.

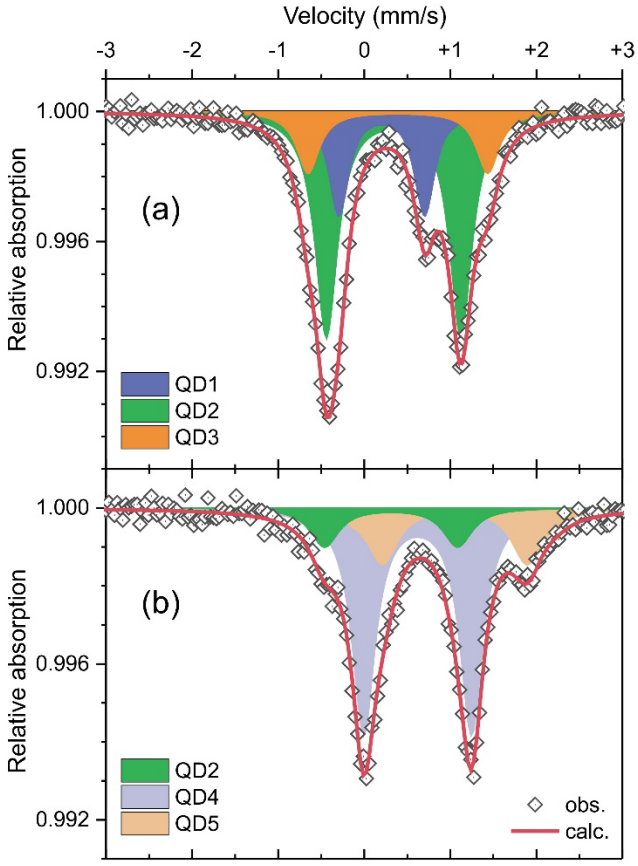

Figure 12: ^{57}Fe Mössbauer spectra of (a) Fe^{III}(¼)HA and (b) Fe^{II}(¼)HA samples (annealed at 1200°C) recorded at 100 K.

The Mössbauer spectrum of the sample prepared from iron(II) precursor (Figure 12b) can also be described as the sum of three components (labelled QD2, QD4 and QD5) with isomer shift equal to 0.31, 0.62 and 1.05 mm/s, respectively (Table 3). Thus, the QD2 component, which is similar to the QD2 doublet observed for the Fe^{III}(¼)HA sample, clearly reveals the presence of high spin iron (III) in a tetrahedral site, confirming the EPR and XRD results. The two other components (QD4 and QD5) are clearly associated with Fe^{2+} ions. The low value of the isomer shift of the QD4 quadrupole doublet (0.62 mm/s at 100 K) is consistent with high spin Fe^{2+} ions in [2+x] linear

coordination while the third component with isomer shift value of 1.05 mm/s (QD5) arises from four-fold coordinated high spin Fe^{2+} ions. Indeed, in phosphates or oxides the isomer shift ranges for four-fold, five-fold and six-fold coordinated high spin iron (II) are about 1.00 - 1.10, 1.20 -1.26 and 1.28 - 1.39 mm/s (at 100 K), respectively [34]. Considering that iron(II) with such coordination (4 or 4(+1)) can only be found nearby the calcium atoms, this shows that a minor amount of Fe^{2+} ions can substitute Ca^{2+} ions. Moreover, the relative absorption area of the QD4 quadrupole doublet associated with Fe^{2+} ion in [2+x] coordination (63% at 100 K) shows that iron is mainly located in the center of the HA tunnel II, in perfect agreement with the structural refinements from X-ray diffraction data.

Table 3: Refined hyperfine parameters of the different components (QD) used to describe the ^{57}Fe Mössbauer spectra of Fe^{III}(¼)HA and Fe^{II}(¼)HA samples recorded at 100 K. (δ isomer shift relative to α-Fe at 293 K, Δ quadrupole splitting, Γ Lorentzian linewidth and A_r relative area)

	δ (mm/s)	Δ (mm/s)	Γ (mm/s)	A_r (%)	Assignment
FeIII(¼)HA					
QD1	0.20(1)	1.00(2)	0.28(3)	24(3)	HS-Fe^{3+} [2+x]
QD2	0.34(1)	1.56(2)	0.32(3)	60(3)	HS-Fe^{3+} [4]
QD3	0.39(2)	2.09(5)	0.32(5)	16(3)	HS-Fe^{3+} [5]
FeII(¼)HA					
QD2	0.31(3)	1.55(6)	0.40(5)	14(3)	HS-Fe^{3+} [4]
QD4	0.62(1)	1.26(1)	0.33(2)	63(3)	HS-Fe^{2+} [2+x]
QD5	1.05(2)	1.70(3)	0.43(5)	23(3)	HS-Fe^{2+} [4]

Conclusion.

Calcium hydroxyapatite (HA), a key phosphate in bone reconstruction, biocompatible and bioactive, could get osteoconductive properties increased from iron dopant. Nevertheless, it is crucial to well characterize both oxidation state and ion localisation of the iron dopant. For such a propose, two sample series with same general chemical formula: $Ca_{10}(PO_4)_6Fe_xO_yH_z$ were studied.

The first sample series, obtained from co-sintering process of hematite and pure HA (see experimental part) under air leads to Fe^{3+}-doped HA phase, shown as pure phase with $x \leq 0.25$, and then, for higher iron concentration, with calcium-rich phosphate impurities due to the calcium substitution from the ferric dopant into the HA structural network. Indeed, the main part of the Fe^{3+} ions are shown to be in substitution of one calcium Ca(2) atom and one proton, near the HA tunnel II center, into a distorted penta-coordinated site within two shorts bonds, two intermediate length bonds, and one long bond. Consequently, complex Mössbauer and EPR signals (with multiple components) are observed.

The second samples series, obtained from the co-sintering of iron(II) acetate and pure HA under argon leads to pure doped-HA phases for $x \leq 1$. The obtained phases exhibit mainly Fe^{2+} ions but also a minor part of Fe^{3+} ions despite the annealing treatment performed in low $P(O_2)$ partial pressure (10^{-5} bar). Fe^{2+} ions are clearly in substitution of the protons located in the tunnel II axis. Ferrous cations being so located into a [2+x] linear coordination site. The associated deprotonation (charge compensation mechanism) is clearly demonstrated from NMR and FTIR spectroscopies, and the localization of ferrous ions in the dumbbell site is well demonstrated coupling X-ray diffraction pattern refinements, EPR and Mössbauer spectra analyses.

It can be noted that the use of Fe_3O_4 precursor (i.e., with both ferrous and ferric ions) leads to a combination of the local environments observed in the two reported sample series. This confirms that the iron oxidation state is well the key parameter governing the dopant location and charge compensation mechanism (calcium ion removing and/or deprotonation) inside the HA structural framework.

Acknowledgements

The authors thanks to the French regional council of Nouvelle Aquitaine for the financial funding given to this study. This work benefited from French government support managed by the National Research Agency under the Investments for the future program with the reference ANR-10-LABX-0074-01 Sigma-LIM.

The authors wish to express their sinere gratitude to Professor Jean-Marc Grenèche from Le Mans University, for his insightful comments about this work and his valuable assistance with the Mössbauer data analysis.

References

[1] R.Z. LeGeros, J.P. LeGeros, Dense hydroxyapatite, in *An Introduction to Bioceramics*, World Scientific, **1993**, 139-180.

[2] M. Jiang, J. Terra, A.M. Rossi, M.A. Morales, E.M.B. Saitovitch, D.E. Ellis, Fe^{2+}/Fe^{3+} substitution in hydroxyapatite: Theory and experiment, *Phys. Rev. B*, **2002**, *66*, 224107.

[3] M.S.-A. Johnsson, G.H. Nancollas, The role of brushite and octacalcium phosphate in apatite formation, *Crit. Rev. Oral Biol. Med.*, **1992**, *3*, 61-82.

[4] S. Bose, G. Fielding, S. Tarafder, A. Bandyopadhyay, Understanding of dopant-induced osteogenesis and angiogenesis in calcium phosphate ceramics, *2013*, *31*, 594-605.

[5] H.-M. Yun, S-J. Ahn, K.-R. Park , M.-J. Kim, J.-J. Kim, G.-Z. Jin, H.-W. Kim, E.-C. Kim, Magnetic nanocomposite scaffolds combined with static magnetic field in the stimulation of osteoblastic differentiation and bone formation, *Biomaterials*, **2016**, *85*, 88-98.

[6] G.A. Gamal, F.A. Al-Mufadi, A.H. Said, Effect of iron additives on the microstructure of hydroxyapatite, **2013**, 3, 532-539.

[7] K. A. Gross, R. Jackson, J.D. Cashion, L.M. Rodriguez-Lorenzo, Iron substituted apatites: a resorbable biomaterial with potential magnetic properties, *Eur. Cell. Mater.*, **2002**, *3*, 114-117.

[8] A. Kyriacou, T. Leventouri, B. C. Chakoumakos, V. O. Garlea, et K. D. Sorge, Combined X-ray and neutron diffraction Rietveld refinement in iron-substituted nano-hydroxyapatite, *J Mater Sci*, **2013**, *48*, 3535-3545.

[9] Y. Li, C.T. Nam, C.P. Ooi, Iron(III) and manganese(II) substituted hydroxyapatite nanoparticles: Characterization and cytotoxicity analysis, *J. Phys. Conf. Ser.*, **2009**, *187*, 012024.

[10] H. R. Low, N. Phonthammachai, A. Maignan, G.A. Stewart, T.J. Bastow, L.L. Ma, T.J. White, The crystal chemistry of ferric oxyhydroxyapatite, *Inorg. Chem.*, **2008**, *47*, 11774-11782.

[11] L. Sheikh, S. Sinha, Y.N. Singhababu, V. Verma, S. Tripathy, S. Nayar, Traversing the profile of biomimetically nanoengineered iron substituted hydroxyapatite: synthesis, characterization, property evaluation, and drug release modeling, *RSC Adv.*, **2018**, *8*, 19389-19401.

[12] B. Singh, A. Tandon, A.K. Pandey, P. Singh, Enhanced dielectric constant and structural transformation in Fe-doped hydroxyapatite synthesized by wet chemical method, *J. Mater. Sci.*, **2018**, *53*, 8807-8816.

[13] A. Tampieri, T. D'Alessandro, M.S. Sprio, E. Landi, L. Bertinetti, S. Panseri, G. Pepponi, J. Goettlicher, M. Bañobre-López, J. Rivas, Intrinsic magnetism and hyperthermia in bioactive Fe-doped hydroxyapatite, *Acta Biomater.*, **2012**, *8*, 843-851.

[14] J. Wang, T. Nonami, K. Yubata, Syntheses, structures and photophysical properties of iron containing hydroxyapatite prepared by a modified pseudo-body solution, *J. Mater. Sci. Mater. Med.*, **2008**, *19*, 2663-2667.

[15] H.-C. Wu, T.-W. Wang, J.-S. Sun, W.-H. Wang, F.-H. Lin, « A novel biomagnetic nanoparticle based on hydroxyapatite », *Nanotechnology*, **2007**, *18*, 165601.

[16] K.-H. Zuo, Y.-P. Zeng, D. Jiang, Synthesis and magnetic property of iron ions-doped hydroxyapatite, *J. Nanosci. Nanotechnol.*, **2012**, *12*, 7096-7100.

[17] B. Sutter, D. W. Ming, A. Clearfield, L. R. Hossner, Mineralogical and chemical characterization or iron-, manganese, and copper-containing synthetic hydroxyapatites, *Soil Sci Soc Am J*, **2003**, *67*, 1935-1942.

[18] G. Salviulo, M. Bettinelli, U. Russo, A. Speghini, L. Nodari, Synthesis and structural characterization of Fe^{3+}-doped calcium hydroxyapatites: role of precursors and synthesis method, *J Mater Sci*, **2011**, *46*, 910-922..

[19] S. Kato, S. Ikeda, K. Saito, M. Ogasawara, Fe incorporation into hydroxyapatite channels by Fe loading and post-annealing, *J. Solid State Chem.*, **2018**, *265*, 411-416.

[20] S. Gomes, A. Kaur, J.M. Grenèche, J. M. Nedelec, G. Renaudin, Atomic scale modeling of iron-doped biphasic calcium phosphate bioceramics, *Acta Biomater.*, **2017**, *50*, 78-88.

[21] S. Raynaud, E. Champion, D. Bernache-Assollant, P. Thomas, Calcium phosphate apatites with variable Ca/P atomic ratio I. Synthesis, characterisation and thermal stability of powders, *Biomaterials*, **2002**, *23*, 1065-1072.

[22] A. Hauser, Ligand field theoretical considerations in *Topics in Current Chemistry*, **2004**, 49-58.

[23] N. Pailhe, A. Wattiaux, M. Gaudon, A. Demourgues, Correlation between structural features and vis–NIR spectra of α-Fe_2O_3 hematite and AFe_2O_4 spinel oxides (A = Mg, Zn), *J. Solid State Chem.*, **2008**, *181*, 1040-1047.

[24] P. Prokůpková, L. Koudelka, P. Mošner, Study of the system $FePO_4$-$FeVO_4$ prepared from the solution, *J. Mater. Sci.*, **1996**, *31*, 3391-33955.

[25] I. Rychlowska-Himmel, P. Tabero, Phase equilibri in the system V_2O_5–$Fe_8V_{10}W_{16}O_{85}$ and some properties of the $Fe_8V_{10}W_{16}O_{85}$ phase, *J. Therm. Anal. Calorim.*, **2001**, *65*, 537-543.

[26] S.-J. Bae, J.A Park, J.-J. Lee, G.-H. Lee, T.-J. Kim, D.-S. Yoo, Y. Chang, Ultrasmall iron oxide nanoparticles: Synthesis, physicochemical, and magnetic properties », *Curr. Appl. Phys.*, **2009**, *9*, 19-21.

[27] K. Zaghib, C.M. Julien, Structure and electrochemistry of $FePO_4 \cdot 2H_2O$ hydrate, *J. Power Sources*, **2005**, *142*, 279-284.

[28] M. Maccario, L. Croguennec, B. Desbat, M. Couzi, F. L. Cras, et L. Servant, Raman and FTIR spectroscopy investigations of carbon-coated Li_xFePO_4 materials, *J. Electrochem. Soc.*, **2008**, *155*, 879-886.

[29] S.V. Stefanovsky, O.I. Stefanovsky, M.B. Remizov, E.A. Belanova, P.V. Kozlov, Y.S. Glazkova, A.V. Sobolev, I.A. Presniakov, S.N. Kalmykov, B.F. Myasoedov, FTIR and Mössbauer spectroscopic study of sodium–aluminum–iron phosphate glassy materials for high level waste immobilization », *J. Nucl. Mater.*, **2015**, *466*, 142-149.

[30] J. C. Elliott, Hydroxyapatite and nonstoichiometric apatites, in *Structure and chemistry of the apatites and other calcium orthophosphates*, Elsevier, **1994**, *18*, 111-189.

[31] P. Hartmann, C. Jäger, St. Barth, J. Vogel, K. Meyer, Solid state NMR, X-Ray diffraction, and infrared characterization of local structure in heat-treated oxyhydroxyapatite microcrystals: An analog of the thermal decomposition of hydroxyapatite during plasma-spray procedure, *J. Solid State Chem.*, **2001**, *160*, 460-468.

[32] R. M. Golding, M. Kestigian, C. W. Tennant, EPR of high-spin Fe^{3+} in calcium tungstate, $CaWO_4$, *J. Phys. C Solid State Phys.*, **1978**, *11*, 5041-5049.

[33] D.H. Lin, G. Coudurier, J.C. Vedrine, Fe-ZSM-5: Physicochemical and catalytic properties, in *Studies in Surface Science and Catalysis*, Elsevier, **1989**, *49*, 1431-1448.

[34] J. Peisach, W. E. Blumberg, E. T. Lode, M. J. Coon, An Analysis of the Electron Paramagnetic Resonance Spectrum of Pseudomonas oleovorans Rubredoxin, *J. Biol. Chem.*, **1971**, *246*, 5877-5881.

[35] S. Dzwigaj, L. Stievano, F. E. Wagner, M. Che, Effect of preparation and metal content on the introduction of Fe in BEA zeolite, studied by DR UV-vis, EPR and Mössbauer spectroscopy. *J Phys. Chem. Solids*, **2007**, *68*, 1885-1891.

[36] M. Santhosh Kumar, M. Schwidder, W. Grünert, A. Brückner, On the nature of different iron sites and their catalytic role in Fe-ZSM-5 DeNOx catalysts: new insights by a combined EPR and UV/VIS spectroscopic approach. *J. Catal.*, **2004**, *227*, 384-397.

[37] V. Vercamer, G. Lelong, H. Hijiya, Y. Kondo, L. Galoisy, G. Calas Diluted Fe3+ in silicate glasses: Structural effects of Fe-redox state and matrix composition. An optical absorption and X-band/Q-band EPR study. *J. Non-Cryst. Solids*, **2018**, *428*, 138-145.

[38] F. Menil Systematic trends of the ^{57}Fe Mössbauer isomer shifts in (FeO_n) and (FeF_n) polyhedral. Evidence of a new correlation between the isomer shift and the inductive effect of the competing bond *T-X* (→Fe) (where *X* is O or F and *T* any element with formal positive charge). *J. Phys. Chem. Solids*, **1985**, *46*, 763-789.

[39] S. Gomes, A. Kaur, J.-M. Greneche, J.-M. Nedelec, G. Renaudin Atomic scale modelling of iron-doped biphasic calcium phosphate bioceramics. *Acta Biomater.*, **2017**, *50*, 78-88.

For Table of Contents only

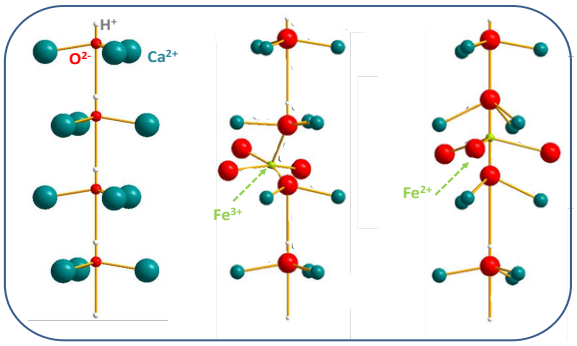

Fe^{2+}- and Fe^{3+}-doped hydroxyl apatite were successfully prepared with potentially improved osteoconduction from a solid state synthesis route. Doping effect on unit-cell parameters versus temperatures was deeply investigated. Especially, Fe^{2+} and Fe^{3+} positioning inside the HA crystallographic framework (x, y z, positions and geometry of the coordination sites) and the ionic substitution compensation mechanism (charge conservation) for both ferrous and ferric dopants were resolved coupling XRD pattern refinement, NMR, EPR and Mossbauer spectroscopies.